The role of Wigner Distribution Function in Non-Line-of-Sight Imaging

Xiaochun Liu*, *Member, IEEE,* Andreas Velten, *Member, IEEE*

Abstract—Non-Line-of-Sight imaging has been linked to wave diffraction by the recent phasor field method. In wave optics, the Wigner Distribution Function description for an optical imaging system is a powerful analytical tool for modeling the imaging process with geometrical transformations. In this paper, we focus on illustrating the relation between captured signals and hidden objects in the Wigner Distribution domain. The Wigner Distribution Function is usually used together with approximated diffraction propagators, which is fine for most imaging problems. However, these approximated diffraction propagators are not valid for Non-Line-of-Sight imaging scenarios. We show that the exact phasor field propagator (Rayleigh-Sommerfeld Diffraction) does not have a standard geometrical transformation, as compared to approximated diffraction propagators (Fresnel, Fraunhofer diffraction) that can be represented as shearing or rotation in the Wigner Distribution Function domain. Then, we explore differences between the exact and approximated solutions by characterizing errors made in different spatial positions and acquisition methods (confocal, non-confocal scanning). We derive a lateral resolution based on the exact phasor field propagator, which can be used as a reference for theoretical evaluations and comparisons. For targets that lie laterally outside a relay wall, the loss of resolution is geometrically illustrated in the context of the Wigner Distribution Function.

Index Terms—Non-Line-of-Sight Imaging, Wigner Distribution Function, Computational Imaging

1 Introduction

None-Line-of-Sight (NLOS) time-resolved imaging uses fast illumination from reflections off a relay surface and detectors to measure signals of an occluded scene. It then uses those captured signals to recover an image around the corner via computational methods.

After a theoretical exploration of ultra-fast NLOS imaging [1], [2], Velten *et al.* first demonstrate experiments in NLOS imaging using a femtosecond laser and streak camera with a filtered backprojection (FBP) algorithm. This FBP method is shown to be similar to the solution of a computed tomography problem [3], [4]. NLOS imaging using a gated Single-Photon Avalanche Diode (SPAD) has been demonstrated by Buttafava *et al.* [5], and a picosecond laser and SPAD experimental setup are currently widely used in time-resolved NLOS imaging scenarios [6], [7], [8], [9], [10]. Based on acquisition schemes, captured signals are divided into confocal [6] and non-confocal measurements [3]. More about different acquisition schemes with simulated datasets can be found [11].

Liu *et al.* [8] and Reza *et al.* [12] show that NLOS imaging problems can be described using a wave diffraction phasor field model. In the following text, we name it as phasor field NLOS imaging. With the help of the phasor field model, one can study time-resolved NLOS imaging as an optical diffraction problem. Several insightful models of phasor field NLOS imaging, as well as experiments, have been proposed and demonstrated by different groups [13], [14], [15], [16].

In classical optics, the Wigner Distribution Function (WDF) [17] and its Fourier transform pair the Ambiguity Function [18] are powerful analytical tools to study optical diffraction, phase space [19], and partially coherent light [20]. An optical imaging process (such as propagation through a lens or free-space propagations) can be interpreted as a simple geometrical transformation in the WDF domain [21], [22], [23]. This conceptual understanding is also useful in the light field imaging. Several works draw connections between light fields and the Wigner Distribution Function [24], [25], [26], [27].

In phasor field NLOS imaging, the Rayleigh-Sommerfeld Diffraction (RSD) model is shown to be a key solution to Non-Line-of-Sight imaging problems [8]. All existing applications of the Wigner Distribution Function are used when Fresnel approximation is valid. However, in NLOS imaging application, the diffraction happens close to the relay wall where only the RSD holds as an exact solution. This RSD also gives an exact solution to the wave propagation as opposed to the approximations such as Fresnel or Fraunhofer diffraction which are commonly known in classical optics [28], [29], [30]. It is shown that the RSD can be used to solve scanning free, real-time, three-dimensional NLOS reconstruction problem [16]. Dove *et al.* [13] present a two dimensional spatial Wigner Distribution Function in a paraxial region with the approximated Fresnel diffraction for NLOS phasor field model.

The RSD with the Wigner Distribution Function has never been discussed in the context of real-world NLOS measurements. In this paper, we will study the RSD in the Wigner Distribution Function domain and compare it with the Fresnel diffraction under real-world parameters like finite relay wall size, discrete spatial sampling, and different acquisition schemes such as confocal and non-confocal measurements. Another angle to describe our work is to use the Wigner Distribution Function to explain Non-Line-of-Sight imaging and clarify when approximations are useful and meaningful in practice.

The key contributions of this paper are listed below:

- We study Rayleigh-Sommerfeld Diffraction in the Wigner Dis-

- *X. Liu is with the Department of Electrical and Computer Engineering, University of Wisconsin, Madison, WI, 53705. A. Velten is with the Department of Biostatistics and Medical Informatics and Electrical and Computer Engineering, University of Wisconsin, Madison, WI, 53705.*
- **Paper correspondence: Xiaochun Liu (https://xiaochunliu.github.io/). Project webpage: https://xiaochunliu.github.io/nloswdf/*

tribution domain and show that the exact Rayleigh-Sommerfeld Diffraction solution does not have any geometrical interpretations as opposed to the Fresnel approximation which has a shear mapping interpretation in the Wigner Distribution Function domain.

- We derive a lateral resolution limit from the exact Rayleigh-Sommerfeld Diffraction solution for NLOS reconstructions.
- We provide an understanding of spatial sampling for phasor field wavefronts on a relay wall.
- We characterize errors from the Fresnel diffraction. We show that this error is less in the confocal acquisition, which makes it an applicable candidate for reconstruction algorithms. In addition, errors from the confocal acquisition and the non-confocal acquisition are visualized in the Wigner Distribution Function domain.

The first part of this work contains a short review of the Wigner Distribution Function and its description of a linear system in Sec. 2. Then using this linear system Wigner Distribution Function description, we show how the Wigner Distribution Function is being used to model and solve problems in Sec. 3. After that, applications of the theoretical understanding are presented in Sec. 4. The conclusion and discussion section is at the end in Sec. 5.

Related Work

In addition to works mentioned in the Introduction, there are other developments in NLOS imaging.

For works in time-resolved optical picosecond NLOS imaging are listed below. Fast solutions with $n^3 log(n)$ complexity only for confocal [6], [7], and for non-confocal measurements [16]. A different perspective to solve NLOS imaging problem is to use geometrical informations [9], [31]. Iterative solutions [32], [33], [34] are similar to the algebraic reconstruction technique used in the Computed Tomography. However, iterative solutions require a computationally expensive forward model. GPU implementation of backprojection with OpenGL [35] might decrease the computational cost for iterative solutions. Laplacian of Gaussian (LOG) filtered backprojection [36] is similar to the Laplacian filter used in the FBP method [3], but with a Gaussian kernel for denoising. Several works explicitly explore occlusions [37], [38], [39], which can improve the reconstruction quality. Hardware time delay can be used to co-design temporal focusing with reconstructions [40]. To recover a specific room scenario, one can estimate the room by fitting planes from temporal measurements [41]. Unlike recovering an image around the corner, tracking people with less computational resources can be used [42]. Bayesian statistics reconstruction [43] shows that the robustness towards random errors in the measurement, which is a different strategy comparing to all solutions above. Some works aim to provide the simulation dataset with different acquisition methods to NLOS imaging [11] as well as benchmarks [44]. In addition to designing computational methods, color NLOS imaging with single-pixel SPAD sensors had been demonstrated [45], [46]. There are also several works primarily focusing on the analysis for NLOS imaging: feature visibility (missing cone problem) [47], a justification for the filtered backprojection solution [10]. There are also some recent review papers [48], [49] with online recorded presentations [50], [51] which are good start points to catch on current published works.

Methods used in NLOS imaging with a nanosecond temporal resolution, or without temporal resolutions, or non-optical signals are listed below. The inverse method used in the Nanosecond time of flight sensors for a hidden scene reconstruction [52] can be applied to picosecond time resolved measurements. The phasor field wave models [8], [12], [13], [14], [15] can learn more from regular imaging methods, such as optical speckle correlations method [53], speckle for tracking hidden targets [54], passive approach for localization [55], combining with deep learning approach [56], image based tracking [57]. Time resolved NLOS imaging community might also consider combining different signals, such as superheterodyne synthetic wave [58], [59], [60], [61], acoustic [62], mid-infrared speckle [63] and long-wave infrared [64] signals.

Notation Setup

Throughout the entire paper, we use notations as follows. $\mathcal{F}(\cdot)$ stands for the Fourier transform, $W_f(\cdot,\cdot)$ for the Wigner Distribution Function (WDF) where the footnote f refers to an input function. We use integral(s) to describe a linear operator (for example, diffraction throughout this paper). For example, to describe a standard linear operator in space or frequency (input, output spatial/frequency representation), we express the linear integral as follows:

$$f_\mathrm{o}(x_\mathrm{o}) = \int h_{xx}(x_\mathrm{o}, x_\mathrm{i}) f_\mathrm{i}(x_\mathrm{i})\, dx_\mathrm{i}$$
$$F_\mathrm{o}(\mu_\mathrm{o}) = \frac{1}{2\pi} \int h_{\mu\mu}(\mu_\mathrm{o}, \mu_\mathrm{i}) F_\mathrm{i}(\mu_\mathrm{i})\, d\mu_\mathrm{i}\,, \quad (1)$$

In Eq. (1), an input $f_\mathrm{i}(x_\mathrm{i})$ and a output $f_\mathrm{o}(x_\mathrm{o})$ are denoted by footnotes (the same for their frequency representations $F_\mathrm{i}(\mu_\mathrm{i}) = \mathcal{F}(f_\mathrm{i}(x_\mathrm{i}))$, $F_\mathrm{o}(\mu_\mathrm{o}) = \mathcal{F}(f_\mathrm{o}(x_\mathrm{o}))$). For a one dimensional linear operator above, the kernel $h_{xx}(x_\mathrm{o}, x_\mathrm{i})$ in its primary domain x or $h_{\mu\mu}(\mu_\mathrm{o}, \mu_\mathrm{i})$ in its frequency domain μ can be used to describe the relationship between input $f_\mathrm{i}(x_\mathrm{i})$ and output $f_\mathrm{o}(x_\mathrm{o})$ functions (signals). In later sections, $h_{xx}(x_\mathrm{o}, x_\mathrm{i})$ is used to describe a wave propagation which is tied to a physical diffraction process.

We list the most frequently used notations below:

- $\mathcal{F}(\cdot)$: Fourier transform
- $f_\mathrm{i}(x_\mathrm{i})$/$F_\mathrm{i}(\mu_\mathrm{i})$: Input spatial/frequency representation
- $f_\mathrm{o}(x_\mathrm{o})$/$F_\mathrm{o}(\mu_\mathrm{o})$: Output spatial/frequency representation
- $f^*(x)$/$F^*(\mu)$: Complex conjugate of spatial/frequency representation
- $h_{xx}(x_\mathrm{o}, x_\mathrm{i})$: Linear operator spatial integral kernel
- $h_{xx}(x)$: Linear operator spatial convolution kernel
- $h_{\mu\mu}(\mu_\mathrm{o}, \mu_\mathrm{i})$: Linear operator frequency integral kernel
- $\mathcal{W}_{f_\mathrm{i}}(x_\mathrm{i}, \mu_\mathrm{i})$: Input Wigner Distribution Function for object f_i.
- $\mathcal{W}_{f_\mathrm{o}}(x_\mathrm{o}, \mu_\mathrm{o})$: Output Wigner Distribution Function for object f_o.
- $\underset{x-y}{*}$: A convolution along both $x-y$ dimension.

Abbreviations: Wigner Distribution Function (WDF), Rayleigh-Sommerfeld Diffraction (RSD), Single-Photon Avalanche Diode (SPAD), Non-Line-of-Sight (NLOS) imaging.

2 Wigner Distribution Function in Classical Imaging

Most imaging phenomena can be (approximately) described by the linearity of coherent wave or its intensity and formulated as linear operators. In this section, we review the linear operator in the WDF domain in a formula cookbook fashion [22], [23], [65]. Then we apply this WDF framework to show the RSD and Fresnel diffraction (RSD, Fresnel propagators) in the WDF domain.

2.1 Wigner Distribution Function Representation

To describe a physical object, its spatial $f(x)$ (x refers to the spatial coordinate) and spatial frequency $F(\mu)$ signal representations can be converted through the Fourier transform. For example, $f(x)$ can be a image on the x coordinate and $F(\mu)$ refers to its Fourier transform. In a word, a standard way to present this object is either in the space **or** in the spatial frequency domain. However, WDF $\mathcal{W}_f(x,\mu)$ gives us both space **and** spatial frequency representation for this object which is different from the Fourier transform.

The WDF $\mathcal{W}_f(x,\mu)$ of this object f can be calculated through its $f(x)$ or $F(\mu)$ is given below:

$$\mathcal{W}_f(x,\mu) = \int_{-\infty}^{+\infty} \underbrace{f(x+\frac{\tau}{2})\, f^*(x-\frac{\tau}{2})}_{\text{Spatial representation}}\, e^{-j2\pi\mu\tau} d\tau$$
$$= \int_{-\infty}^{+\infty} \underbrace{F(\mu+\frac{\xi}{2})\, F^*(\mu-\frac{\xi}{2})}_{\text{Spatial frequency representation}}\, e^{j2\pi x\xi} d\xi\,, \tag{2}$$

$\mathcal{W}_f(x,\mu)$ in Eq. (2) is a function of both space x and spatial frequency μ for a one dimensional object f. Overall, the Wigner Distribution Function representation always doubles the dimension for the notation of an object (1d signals have 2d WDF, 2d signals have 4d WDF).

2.2 Linear Operators in the Wigner Distribution Function Domain

Given an integral expression in space or frequency for a linear operator, the skeleton for this linear operator in the WDF domain can be derived immediately [22], [23], [65]. For example, a linear system can be described as a linear operator to describe wave propagation in the context of wave optics. For simplicity, we use a one-dimensional linear operator as an example in this section.

The linear system WDF description aims to build a relationship between an input WDF $\mathcal{W}_{f_\mathrm{i}}(x_\mathrm{i},\mu_\mathrm{i})$ and a output WDF $\mathcal{W}_{f_\mathrm{o}}(x_\mathrm{o},\mu_\mathrm{o})$ by using a four dimensional kernel $K(x_\mathrm{o},\mu_\mathrm{o},x_\mathrm{i},\mu_\mathrm{i})$. Intuitively speaking, it tries to capture how a transformation effects in both space and spatial frequency domains.

$$\mathcal{W}_{f_\mathrm{o}}(x_\mathrm{o},\mu_\mathrm{o}) = \frac{1}{2\pi}\iint K(x_\mathrm{o},\mu_\mathrm{o},x_\mathrm{i},\mu_\mathrm{i})\mathcal{W}_{f_\mathrm{i}}(x_\mathrm{i},\mu_\mathrm{i})\, dx_\mathrm{i} d\mu_\mathrm{i}\,, \tag{3}$$

$K(x_\mathrm{o},\mu_\mathrm{o},x_\mathrm{i},\mu_\mathrm{i})$ in Eq. (3) links an input object $\mathcal{W}_{f_\mathrm{i}}(x_\mathrm{i},\mu_\mathrm{i})$ and a output object $\mathcal{W}_{f_\mathrm{o}}(x_\mathrm{o},\mu_\mathrm{o})$ in the WDF domain. Once we know a spatial $h_{xx}(x_\mathrm{o},x_\mathrm{i})$ or a frequency description $h_{\mu\mu}(\mu_\mathrm{o},\mu_\mathrm{i})$ (notations are stated in Eq. (1)) for a linear system, we can derive the associated $K(x_\mathrm{o},\mu_\mathrm{o},x_\mathrm{i},\mu_\mathrm{i})$ in Eq. (3) as follows,

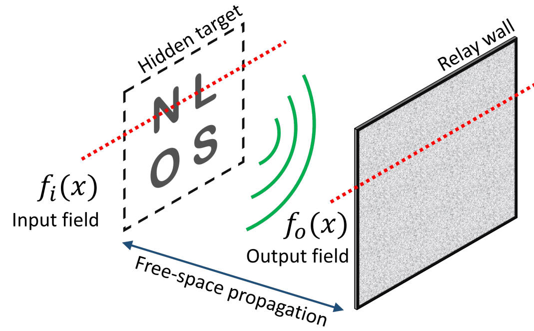

Fig. 1. Two parallel planes (lines) setup geometry in Sec. 2.3. $f_\mathrm{i}(x)$ and $f_\mathrm{o}(x)$ represent line slices of the field used in Eq. (5).

$$\begin{aligned} &K(x_\mathrm{o},\mu_\mathrm{o},x_\mathrm{i},\mu_\mathrm{i}) = \\ &:= \iint h_{xx}(x_\mathrm{o}+\frac{x_\mathrm{o}^{'}}{2}, x_\mathrm{i}+\frac{x_\mathrm{i}^{'}}{2})\, h_{xx}^*(x_\mathrm{o}-\frac{x_\mathrm{o}^{'}}{2}, x_\mathrm{i}-\frac{x_\mathrm{i}^{'}}{2}) \\ &\quad \exp\Big[-j\mu_\mathrm{o}x_\mathrm{o}^{'} + j\mu_\mathrm{i}x_\mathrm{i}^{'}\Big]\, dx_\mathrm{o}^{'} dx_\mathrm{i}^{'} \\ &:= (\frac{1}{2\pi})^2 \iint h_{\mu\mu}(\mu_\mathrm{o}+\frac{\mu_\mathrm{o}^{'}}{2}, \mu_\mathrm{i}+\frac{\mu_\mathrm{i}^{'}}{2})\, h_{\mu\mu}^*(\mu_\mathrm{o}-\frac{\mu_\mathrm{o}^{'}}{2}, \mu_\mathrm{i}-\frac{\mu_\mathrm{i}^{'}}{2}) \\ &\quad \exp\Big[j\mu_\mathrm{o}^{'}x_\mathrm{o} - j\mu_\mathrm{i}^{'}x_\mathrm{i}\Big]\, d\mu_\mathrm{o}^{'} d\mu_\mathrm{i}^{'}\,, \end{aligned} \tag{4}$$

Eq. (3) and Eq. (4) can be adapted to any linear operators with $h_{xx}(x_\mathrm{o},x_\mathrm{i})$ (or $h_{\mu\mu}(\mu_\mathrm{o},\mu_\mathrm{i})$) in analytical forms. Notice that $K(x_\mathrm{o},\mu_\mathrm{o},x_\mathrm{i},\mu_\mathrm{i})$ is completely described the linear physical process. Constraints on variables $(x_\mathrm{o},\mu_\mathrm{o},x_\mathrm{i},\mu_\mathrm{i})$ can be made to model this linear physical process even more (such as an energy constraint, a frequency bandwidth, and a spatial truncation). Some special linear systems directly have closed-form expressions without deriving by definitions from Eq. (3) and Eq. (4).

2.3 Diffraction in the Wigner Distribution Function Domain

In this section, we describe the RSD and Fresnel diffraction in the WDF domain by using formulas in Sec.2.2. These two diffraction propagators are related to the NLOS imaging problem.

Before deriving the RSD and Fresnel diffraction in the WDF domain, we need to introduce a notation setup for this section. For simplicity, in the one-dimensional Cartesian coordinate system, we consider two parallel lines with a spacing z (distance between lines). The geometrical setup is shown in Fig. 1. Spatial representations for $h_{xx}^{\mathrm{RSD}}(x_\mathrm{o},x_\mathrm{i})$ (RSD) and $h_{xx}^{\mathrm{Fre}}(x_\mathrm{o},x_\mathrm{i})$ (Fresnel) are used to describe the propagation from an input field $f_\mathrm{i}(x_\mathrm{i})$ to a output field $f_\mathrm{o}(x_\mathrm{o})$. In order to derive the RSD and Fresnel diffraction in the WDF domain, the first step is to write down $h_{xx}(x_\mathrm{o},x_\mathrm{i})$ in an analytical form, then plugging $h_{xx}(x_\mathrm{o},x_\mathrm{i})$ into Eq. (3) and Eq. (4) leads to WDF descriptions for the RSD and Fresnel diffraction.

The first step is to review a standard way of describing the RSD and Fresnel diffraction in the space domain. Both the RSD and the Fresnel diffraction in this geometrical parallel plane setup case, can be treated as a spatial convolution [29], [66], [67]. Thus, it reduces one variable $x = x_\mathrm{o} - x_\mathrm{i}$ for the kernel from

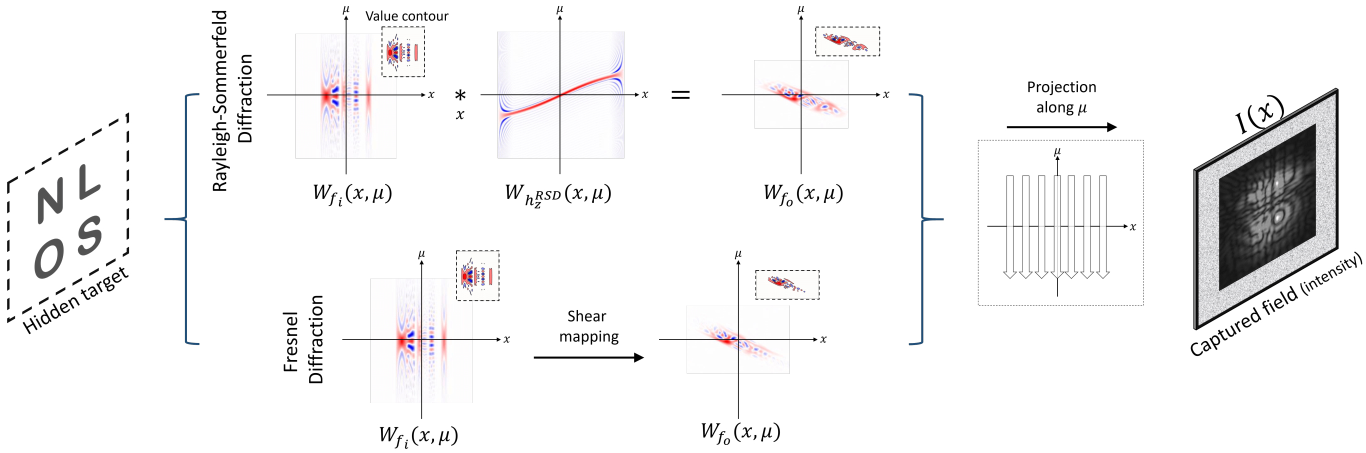

Fig. 2. The RSD and Fresnel diffraction in the WDF domain Eq. (10). $\mathcal{W}_{f_\mathrm{i}}(x,\mu)$ and $\mathcal{W}_{f_\mathrm{o}}(x,\mu)$ are WDF for the input field $f_\mathrm{i}(x)$ and the output field $f_\mathrm{o}(x)$ in Fig. 1. The RSD in the WDF domain is shown in the first row and the Fresnel is in the second row. Both propagators starts from a same target field WDF $\mathcal{W}_{f_\mathrm{i}}(x,\mu)$, the differences lie in transformations in the WDF domain. The RSD refers to a convolution along spatial coordinate x with WDF of the RSD kernel $\mathcal{W}_{h_z^{\mathrm{RSD}}}(x_\mathrm{i},\mu)$ in Eq. (8). The Fresnel diffraction refers to a shear mapping in Eq. (9). We also plot the corresponding value contours (level) for each WDF plot which are shown in dash windows.

$h_{xx}(x_\mathrm{o},x_\mathrm{i})$ to $h_{xx}(x)$ in Eq. (5). We use notation $\underset{x}{*}$ to represent the convolution along x dimension.

$$f_\mathrm{o}(x_\mathrm{o}) = f_\mathrm{i}(x_\mathrm{i}) * h_{xx}(x_\mathrm{o},x_\mathrm{i}) := f_\mathrm{i}(x_\mathrm{i}) \underset{x}{*} h_{xx}(x)\,, \tag{5}$$

For the RSD, $h_{xx}(x)$ refers to:

$$h_{xx}(x) = h_{xx}^{\mathrm{RSD}}(x) = \frac{e^{jk\sqrt{x^2+z^2}}}{\sqrt{x^2+z^2}} \tag{6}$$

For the Fresnel diffraction, $h_{xx}(x)$ refers to:

$$h_{xx}(x) = h_{xx}^{\mathrm{Fre}}(x) = \frac{e^{jkz}}{j\lambda z} e^{\frac{jk}{2z}x^2} = \alpha(z) e^{\frac{jk}{2z}x^2}\,, \tag{7}$$

$k = \omega/c$ in both cases stand for the wavenumber of a monochromatic wave, which ω refers to the angular frequency and c means the speed of light travelling in air. z refers to the propagation distance (The spacing between an input and a output plane).

The next step is to show the RSD and the Fresnel diffraction in the WDF domain. Given a spatial kernel description $h_{xx}(x_\mathrm{o},x_\mathrm{i})$ either from the RSD or the Fresnel diffraction, we can plug Eq. (6 & 7) into Eq. (4) to calculate the corresponding kernel $K(x_\mathrm{o},\mu_\mathrm{o},x_\mathrm{i},\mu_\mathrm{i})$. Then, we use Eq. (3) to link input WDF $\mathcal{W}_{f_\mathrm{i}}(x_\mathrm{i},\mu)$ with output WDF $\mathcal{W}_{f_\mathrm{o}}(x_\mathrm{o},\mu)$ by $K(x_\mathrm{o},\mu_\mathrm{o},x_\mathrm{i},\mu_\mathrm{i})$. Thus, we achieve WDF descriptions for the RSD and the Fresnel diffraction. We skip algebraic steps here, calculations are provided in Appendix 6.1.

The RSD and the Fresnel diffraction in the WDF domain are given below. $\mathcal{W}_{f_\mathrm{i}}(x_\mathrm{i},\mu)$ and $\mathcal{W}_{f_\mathrm{o}}(x_\mathrm{o},\mu)$ stand for the WDF of an input and a output wavefront.

- **RSD in the WDF domain** in Eq. (8) refers to a convolution along the spatial x direction. $\mathcal{W}_{h_z^{\mathrm{RSD}}}(x_\mathrm{i},\mu)$ stands for the WDF of the RSD convolution kernel $h_z^{\mathrm{RSD}}(x) = \frac{e^{jk\sqrt{x^2+z^2}}}{\sqrt{x^2+z^2}}$ where a footnote z denotes a propagating distance.

$$\begin{aligned}\mathcal{W}_{f_\mathrm{o}}(x_\mathrm{o},\mu) &= \mathcal{W}_{h_z^{\mathrm{RSD}}}(x_\mathrm{i},\mu) \underset{x}{*} \mathcal{W}_{f_\mathrm{i}}(x_\mathrm{i},\mu) \\ &:= \int \mathcal{W}_{h_z^{\mathrm{RSD}}}(x_\mathrm{o}-x_\mathrm{i},\mu)\mathcal{W}_{f_\mathrm{i}}(x_\mathrm{i},\mu)\,dx_\mathrm{i}\,,\end{aligned} \tag{8}$$

- **Fresnel diffraction in the WDF domain** in Eq. (9) refers to a shear mapping (coordinate transformation) as a function of a propagating distance z.

$$\mathcal{W}_{f_\mathrm{o}}(x,\mu) = \mathcal{W}_{f_\mathrm{i}}(x - \frac{z}{k}\mu, \mu)\,, \tag{9}$$

Then, an output intensity $I_\mathrm{o}(x_\mathrm{o}) = |f_\mathrm{o}(x_\mathrm{o})|^2$ of the wavefront $f_\mathrm{o}(x_\mathrm{o})$ can be calculated from the marginal distribution of the output WDF $\mathcal{W}_{f_\mathrm{o}}(x_\mathrm{o},\mu)$ (projection along frequency coordinate μ),

$$\begin{aligned}I_\mathrm{o}(x_\mathrm{o}) &= |f_\mathrm{o}(x_\mathrm{o})|^2 \\ &= \int \underbrace{\mathcal{W}_{f_\mathrm{o}}(x_\mathrm{o},\mu)}_{\text{Eq.(8 or 9)}}\,d\mu \quad \text{- projection along } \mu \\ I_\mathrm{o}^{\mathrm{RSD}}(x) &:= \iint \mathcal{W}_{h_z^{\mathrm{RSD}}}(x-x_\mathrm{i},\mu)\mathcal{W}_{f_\mathrm{i}}(x_\mathrm{i},\mu)\,dx_\mathrm{i}\,d\mu \\ I_\mathrm{o}^{\mathrm{Fre}}(x) &:= \int \mathcal{W}_{f_\mathrm{i}}(x - \frac{z}{k}\mu, \mu)\,d\mu\,,\end{aligned} \tag{10}$$

Fig. 2 illustrates calculation steps in Eq. (10). Propagation using the Fresnel diffraction results in shearing of the WDF. Propagation using the exact RSD propagator, however, does not have a simple geometrical interpretation in the WDF domain. In the next section, more details are discussed in the context of NLOS imaging.

3 Wigner Distribution Function in Non-Line-of-Sight Imaging

In this section, we discuss NLOS imaging within the phasor field virtual wave optics and the WDF framework. To understand how the NLOS imaging problem is related to wave optics, we review the phasor field method [8], [12], [13], [14], [15], [16]. Then combining the phasor field framework with WDF descriptions, we derive a spatial lateral resolution limit using the exact RSD solution. We explore differences between confocal and non-confocal measurements, and errors from the Fresnel approximation.

3.1 Phasor Field Model Review

We need to introduce some additional variables to illustrate captured NLOS signals. $g(x, y, t)$ represents a captured time response [a], coordinate (x, y) refers to a spatial location of a detector pixel on a relay wall, t refers to a time index. We assume all time responses $g(x, y, t)$ are captured from a plane relay wall.

First, the phasor field $p(x, y)$ is defined to be a single frequency component of $G(x, y, \omega)$ which $G(x, y, \omega)$ stands for the temporal Fourier transform of the captured time response $g(x, y, t)$. In Eq. (11), $p(x, y)$ can be calculated through the Fourier transform of a convolution in time with a temporal harmonic function $e^{j\omega t}$, or product with a shifted delta $\delta(\xi - \omega)$ in the Fourier domain,

$$\begin{aligned} p(x,y) &= \mathcal{F}(g(x,y,t) \underset{t}{*} e^{j\omega t}) \\ &= G(x,y,\xi) \cdot \delta(\xi - \omega) \end{aligned} \tag{11}$$

The angular frequency variable ω and its associated wavelength λ are connected through the wavenumber $k = \omega/c = 2\pi/\lambda$. Overall, the phasor field $p(x, y)$ is defined to be a single frequency content of each captured time response $g(x, y, t)$ in the Fourier domain.

Then, a NLOS imaging process can be understood as follows: An unknown phasor field $p_{\text{i}}(x, y)$ (input) carrying the object's information propagates to a relay wall, where the phasor field $p_{\text{o}}(x, y)$ is captured (output). The goal for reconstructions is to invert this diffraction process from the captured field $p_{\text{o}}(x, y)$ to have a virtual image representation which ideally is the same as $p_{\text{i}}(x, y)$. This diffraction process from $p_{\text{i}}(x, y)$ to $p_{\text{o}}(x, y)$ can be modeled as the RSD propagator which is shown in [8]. $\alpha(x, y)$ refers to an additional amplitude correction factor.

$$\begin{aligned} p_{\text{o}}(x,y) &= \alpha(x,y)\Big(p_{\text{i}}(x,y) \underset{x-y}{*} h_{xx}^{\text{RSD}}(x,y,z)\Big) \\ &\propto p_{\text{i}}(x,y) \underset{x-y}{*} h_{xx}^{\text{RSD}}(x,y,z) \end{aligned} \tag{12}$$

$h_{xx}^{\text{RSD}}(x, y, z)$ in Eq.(12) refers to the RSD convolution kernel in two dimensional case as following (one dimension in Eq. (6)),

$$h_{xx}^{\text{RSD}}(x,y,z) = \frac{e^{jk\sqrt{x^2+y^2+z^2}}}{\sqrt{x^2+y^2+z^2}} \tag{13}$$

Next, since Eq. (12) describes the phasor field diffraction at each frequency ω, by using Eq. (11) with different choices of ω, $p_{\text{i}}(x, y, \omega)$ has another frequency dimension. Then, one can extend the model into a space-time broadband propagator [16] for describing the captured space-time signals as following,

$$p_{\text{o}}(x,y,t) = \int_{\omega\in\Omega} e^{j\omega t}\Big(\underbrace{p_{\text{i}}(x,y,\omega) \underset{x-y}{*} h_{xx}(x,y,z)}_{\text{Diffraction function at } \omega}\Big)\, d\omega \tag{14}$$

Here are some additional explanations for Eq.(14):

- Eq. (14) can be used to describe a propagation either from a hidden target to captured signals (forward propagation), or from captured signals to a virtual image (reconstruction).
- $\omega \in \Omega$ stands for a closed frequency interval that is chosen to match the captured system spatial and temporal resolution (resolvable wavefronts). A NLOS picosecond time-resolved system usually has 60 to 70 picosecond temporal resolution, but phasor field wavefronts are limited by the spatial sampling resolution on a relay wall. Given a discrete spatial sampling grid with a spacing Δ on the relay wall (for example $1\,\text{cm}$), phasor field wave components need to be satisfied the half wavelength condition $\lambda_\omega > \Delta/2, \omega = 2\pi c/\lambda_\omega$ [68].
- In Eq.(11), one can also use a temporal illumination convolution kernel function $e^{j\omega_c t}e^{-\frac{t^2}{2\sigma^2}}$ (Gaussian-modulated sinusoidal pulse) to generate the phaosr field $p_{\text{i}}(x, y, \omega) = \mathcal{F}(g(x, y, t) \underset{t}{*} e^{j\omega_c t}e^{-\frac{t^2}{2\sigma^2}})$, then uses Eq.(14) for reconstruction. This Gaussian-modulated sinusoidal pulse models an object that reflects a temporally changing phasor field wavefront which is shown in [8].
- The benefit of using Eq. (14) is that we can study the space-time NLOS signals by decomposing them into diffraction processes at each individual frequency. For example, the diffraction inside Eq. (14), one can approximate $h_{xx}(x, y, z)$ in Eq. (14) by the Fresnel propagator $h_{xx}^{\text{Fre}}(x, y, z)$ instead of the RSD kernel $h_{xx}^{\text{RSD}}(x, y, z)$. So that each frequency component has a geometrical shear mapping transformation in the WDF domain as shown in Eq. (10).

3.2 Spatial Lateral Resolution from Rayleigh Sommerfeld Diffraction

To understand the achievable lateral resolution in NLOS reconstructions, one have to understand the central frequency for the phasor field. Here we provide an example of the phasor field central frequency in a reconstruction pipeline. As we discussed ealier in the previous section for Eq.(14), considering the phasor field coming from a gaussian-modulated sinusoidal pulse $e^{j\omega_c t}e^{-\frac{t^2}{2\sigma^2}}$, ω_c defines the central frequency for the captured phasor field. Lateral resolution is bounded by the diffraction limits at the central frequency ω_c without exploiting optical occlusions in the hidden scene [13]. Next, we want to show the lateral resolution at a central frequency when using the exact RSD propagator given a finite size relay wall.

First, we model a limited size relay wall using an aperture function $T(x, y)$. Generally speaking, this aperture function can be modeled as real or complex functions which is used in optical coded imaging. However, to derive lateral resolution limits, we consider the aperture function as an binary function $T(x, y) \in \{0, 1\}$ in Eq. (15). N stands for the aperture half side length (for example $N = 1$ as a $2\,\text{m}$ by $2\,\text{m}$ scanning wall).

$$T(x,y) = \begin{cases} 1, & \text{if } |x| \le N, |y| \le N \\ 0, & \text{otherwise} \end{cases} \tag{15}$$

a. Across the entire paper, captured time responses (signal) refer to shifted version of raw temporal measurements. This shifting process could be done during the acquisition by calculating a line-of-sight time delay respect to a distance between physical hardware and focused points on the relay wall. More descriptions please refer to [3].

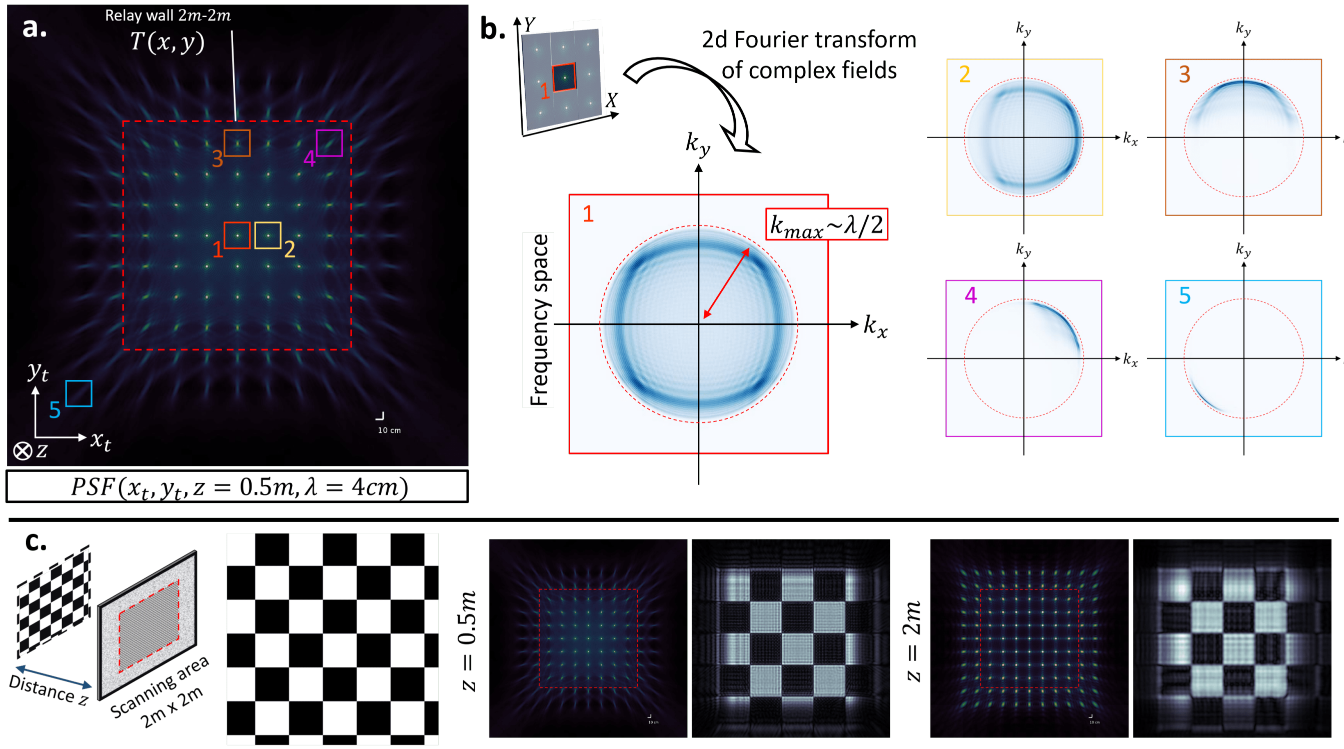

Fig. 3. Achievable lateral resolution from RSD discussed in Sec. 3.2 Eq. (16). **a.** we show the point spread function $PSF(x_t, y_t, z, \omega)$ from multiple point targets in the hidden with $T(x, y)$ ($2\,\mathrm{m}$ by $2\,\mathrm{m}$, red dash box), a target depth $z = 0.5\,\mathrm{m}$ away from a relay wall, a central wavelength $\lambda = 4\,\mathrm{cm}$. Point spread function varies at each lateral location. **b.** we pick five positions (color boxes from 1-5 in **b**) from **a** to illustrate the frequency bandwidth (2d Fourier transform on the complex field). Point position at the center of aperture (number 1, red box) achieves almost maximum bandwidth corresponding to $\lambda/2$. The further away from the center of the aperture, the worse distortion, and the smaller region is covered in the frequency domain. **c.** we show a PSF plot and a reconstructed checkerboard pattern for two depth $z = 0.5\,\mathrm{m}$ - $2\,\mathrm{m}$.

Second, the achievable lateral resolution can be characterized by the point spread function $PSF(x_t, y_t, z, \omega)$ from a point object in the hidden scene at (x_t, y_t, z) shown in Eq. (16). $h(x - x_t, y - y_t, z)$ stands for the scattered phasor field wavefront from a point object with distance z away from the aperture. The multiplication between $T(x, y)$ and $h(x - x_t, y - y_t, z)$ stands for the captured phasor field on the relay wall. $h^*(x, y, z)$ stands for the complex conjugate of the RSD propagation convolution kernel $h(x, y, z) = h^{\mathrm{RSD}}_{xx}(x, y, z)$ shown in Eq. (13).

$$PSF(x_t, y_t, z, \omega) = \left| \Big(\underbrace{\overbrace{T(x, y)}^{\text{Aperture function}} \; \overbrace{h(x - x_t, y - y_t, z)}^{\text{Point object wavefront}}}_{\text{Captured wavefront}} \Big) \underset{x-y}{*} \underbrace{h^*(x, y, z)}_{\text{RSD propagation kernel}} \right|^2 \tag{16}$$

Eq. (16) can be used to calculate the lateral resolution limit as a function of an aperture function $T(x, y)$, the central frequency $\omega_c = 2\pi c/\lambda_c$, the hidden point object position (x_t, y_t, z). The choice of central wavelength λ_c depends on the spatial sampling spacing Δ which is $\lambda_c > \alpha \cdot 2\Delta$ for $\alpha > 1$ in the discussion for Eq. (14) and a system's temporal resolution. Decreasing spatial sampling spacing Δ for a fixed aperture function $T(x, y)$ would lead more spatial sampling points N, but lower the achievable central wavelength λ_c which leads a higher lateral resolution. This central wavelength λ_c is chosen to be at the scale of $4\,\mathrm{cm} \sim 6\,\mathrm{cm}$ with $\Delta = 1\,\mathrm{cm}$ in the previous phasor field experiments [8]. Fig. 3 shows the reconstructed image of multiple point targets that lie in different lateral positions. Fig. 3 plots $PSF(x_t, y_t, z, \omega)$ in Eq. (16) by using a central frequency $\omega_c = 2\pi c/(\lambda_c = 4\,\mathrm{cm})$ with different target depth z settings. We can also study the lateral resolution in the frequency space by applying the Fourier transform to the phasor field $\mathcal{F}\big((T(x, y)h(x - x_t, y - y_t, z)) \underset{x-y}{*} h^*(x, y, z)\big)$ as shown in Fig. 3.

In the WDF domain, when using the Fresnel approximation instead of the RSD to model diffraction, the resolution loss has a more straightforward geometrical explanation. Given an input field WDF $\mathcal{W}_{p_i}(x, \mu)$ and an aperture WDF $\mathcal{W}_T(x, \mu)$, which $T(x) = rect[x] = 1\,(|x| < 1/2), 0\,(\text{otewise})$ is a one dimensional version of Eq. (15), then the output field $\mathcal{W}_{p_o}(x, \mu)$ in the WDF domain is as below,

$$\begin{aligned} \mathcal{W}_{p_o}(x, \mu) &= \underbrace{\mathcal{W}_T(x, \mu)}_{\text{WDF of } T(x)} \underset{\mu}{*} \mathcal{W}_{p_i}(x - \frac{z}{k}\mu, \mu) \\ &= \Big\{ \overbrace{\underbrace{2(1 - |2x|)\, rect[x]}_{\text{spatial truncation}} \; sinc[2(1 - |2x|\mu)]}^{\mathcal{W}_T(x,\mu)} \Big\} \\ &\quad \underset{\mu}{*} \mathcal{W}_{p_i}(x - \frac{z}{k}\mu, \mu) \end{aligned} \tag{17}$$

Eq. (17) uses the WDF Multiplication theorem: the multiplication of $T(x)$ and $p_i(x)$ in the space domain corresponds to the convolution in the Fourier domain which is corresponding to a convolution along the frequency coordinate $\underset{\mu}{*}$ in the WDF domain. The loss of resolution comes from WDF of the aperture function

$\mathcal{W}_T(x,\mu)$ in Eq. (17). Since $\mathcal{W}_T(x,\mu)$ has a truncation term $2(1-|2x|)\,rect[x]$ along the spatial x dimension. Multiplication with $rect[x]$ would result in zero everywhere in the WDF for $x > |\frac{1}{2}|$. For a fixed size scanning aperture, the output field shears more in the WDF domain as the distance z is increasing which causes more loss of information in the frequency domain for the output field WDF $\mathcal{W}_{p_\text{o}}(x,\mu)$. This spatially dependent frequency content is shown in both Fig. 3 and Fig. 6.

3.3 Differences between Confocal and Non-confocal Measurements

The confocal NLOS measurement requires co-locating a SPAD and a laser focused point on a relay wall and sequentially scanning the co-located focused points to measure time responses [6]. Otherwise, general measurement setups are referred to as non-confocal measurements [3]. In this section, we add an illumination wavefront function into the phasor field forward diffraction model, which characterize the differences between the confocal and the non-confocal measurement. We model at the central wavelength λ_c (with angular frequency $\omega_\text{c} = 2\pi c/\lambda_\text{c}$), but the analysis can be applied to each frequency component.

Here are notations would be used in the following. The geometrical setup is shown in Fig. 4 on the left side. We consider a hidden object $f(x,y)$ as an amplitude object at a depth z away from a relay wall (on the $x-y$ plane at $z=0$). For a non-confocal measurement, we have to assign variables (x_i, y_i) to represent a single illumination point source on the relay wall. Collected phasor field wavefronts at the central frequency are denoted by $p_\text{o}^\text{con}(x,y,\omega_\text{c})$ for confocal and $p_\text{o}^\text{n-con}(x,y,\omega_\text{c})$ for non-confocal. The aperture function $T(x,y)$ follows the same notation as in the previous section.

We modify the phasor field forward diffraction model to include two steps [b]: 1. Propagation from a virtual illumination on the relay wall to a target plane. 2. Propagation from the target plane back to the relay wall. For the confocal configuration, the illumination aperture is as the same size as the aperture function. Thus the illumination field can be modeled as a wavefront starting from $T(x,y)$. For the non-confocal configuration, the illumination field is a spherical wavefront starting from a point illumination source at (x_i, y_i) on $x-y$ plane.

For the first step, Eq. (18) calculates the illumination wavefront $u(x,y)$ for confocal $u^\text{con}(x,y)$ and non-confocal $u^\text{n-con}(x,y)$ at the target plane z. $h(x,y,z) = h^\text{RSD}_{xx}(x,y,z)$ refers to Eq. (13),

$$\begin{aligned} u^\text{con}(x,y) &= \left(T(x,y)e^{j\phi(x,y)}\right) \underset{x-y}{*} h(x,y,z) \\ u^\text{n-con}(x,y) &= h(x-x_i, y-y_i, z) \end{aligned} \tag{18}$$

For the second step, the received phasor field wavefront $p_\text{o}(x,y,\omega_\text{c})$ from the hidden object $f(x,y)$ is as follows,

$$\begin{aligned} p_\text{o}(x,y,\omega_\text{c}) &= \iint \underbrace{\overbrace{u(x,y)}^{\text{Illumination}}\ \overbrace{f(x,y)}^{\text{hidden object}}}_{\text{Target wavefront } p_\text{i}(x,y,\omega_c)} h^*(x-\nu, y-\mu, z)\, d\nu\, d\mu \\ &= p_\text{i}(x,y,\omega_\text{c}) \underset{x-y}{*} h^*(x,y,z) \end{aligned} \tag{19}$$

b. As for the confocal measurement, two-way propagation (from illumination to object and object to relay wall) can also be modeled as one-way propagation by thinking the object emits light at the same time but traveling at the half-speed [7].

For the same hidden object $f(x,y)$, confocal and non-confocal measurements *"see"* different unknown target wavefronts $p_\text{i}(x,y,\omega_\text{c})$ because of the illumination wavefront $u(x,y)$ as shown in Eq. (19). More importantly, Eq. (19) also refers that one can probe hidden object's $f(x,y)$ different frequency components by creating illuminating $u(x,y)$ from different spatial points on the relay wall. The reason is as follows. $p_\text{i}(x,y,\omega_\text{c}) = u(x,y)f(x,y)$ comes from the hidden object $f(x,y)$ with a spatial modulation from the illumination wavefront $u(x,y)$. $u(x,y)$ is different between $u^\text{con}(x,y)$ in confocal measurements and $u^\text{n-con}(x,y)$ in non-confocal measurements in Eq. (18). Even for non-confocal measurements from different single illumination points (x_i, y_i), the unknown target field $p_\text{i}(x,y,\omega_\text{c})$ would be different. Based on the Fourier transform multiplication and convolution properties, multiplication in the space $x-y$ domain corresponding to a convolution in the spatial frequency space. Different illumination wavefronts result in different frequency convolution samples on the hidden object $f(x,y)$.

Fig. 4 uses Eq. (19) to show differences between the non-confocal and the confocal measurement in the WDF domain. In Fig. 4, $|\mathcal{W}_{p_\text{o}}^\text{RSD} - \mathcal{W}_{p_\text{o}}^\text{Fre}|(x,\mu)$ shows error maps between the RSD and Fresnel diffraction in the WDF domain. The Fresnel diffraction (shear mapping transform in the WDF domain) works as a better approximation for the confocal acquisition than the non-confocal acquisition. A confocal measurement contains more frequency components of the hidden target than a single illumination non-confocal measurement. This means that reconstructions from confocal data should always look *"sharper"* than reconstructions from single illumination non-confocal data even under the same lab condition. With multiple illumination points, non-confocal measurements can increase frequency components of the hidden target.

3.4 Error Metric for Fresnel Diffraction

Using Fresnel diffraction for reconstructions can be understood as choosing a poor lens with "aberrations" as opposed to use RSD to model a perfect imaging system. The formula to describe the errors made by the Fresnel diffraction can be obtained by replacing the kernel $h^*(x,y,z)$ in Eq. (16) by the Fresnel propagation kernel $h_\text{Fre}(x,y,z) = \alpha(z)e^{\frac{jk}{2z}(x^2+y^2)}$. This focusing error $E(x_t, y_t, z_t, x, y, z)$ is as follows,

$$\begin{aligned} &E(x_t, y_t, z_t, x, y, z) \\ &= \iint \overbrace{T(x,y)}^{\text{Aperture function}}\ \overbrace{h(x-x_t, y-y_t, z_t)}^{\text{Point object wavefront}}\ \overbrace{u(x_t, y_t, z_t)}^{\text{Illumination wavefront}} \\ &\quad \underbrace{h^*_\text{Fre}(x-\nu, y-\mu, z)}_{\text{Fresnel propagation kernel}}\, d\nu\, d\mu \end{aligned} \tag{20}$$

As shown in Eq. (20), the focusing error $E(x_t, y_t, z_t, x, y, z)$ is a six dimensional function. The first three arguments (x_t, y_t, z_t) are from a location of hidden point object and the remaining (x,y,z) are from the Fresnel propagator $h_\text{Fre}(x,y,z)$. Since $E(x_t, y_t, z_t, x, y, z)$ depends on the illumination wavefront $u(x_t, y_t, z_t)$ at the location of hidden target shown in Eq. (18), this error in reconstructions made by the Fresnel diffraction for confocal measurements and non-confocal measurements are different. The behavior of Fresnel diffraction operator varies depending on acquisitions is also provided in Fig. 4 in the WDF domain.

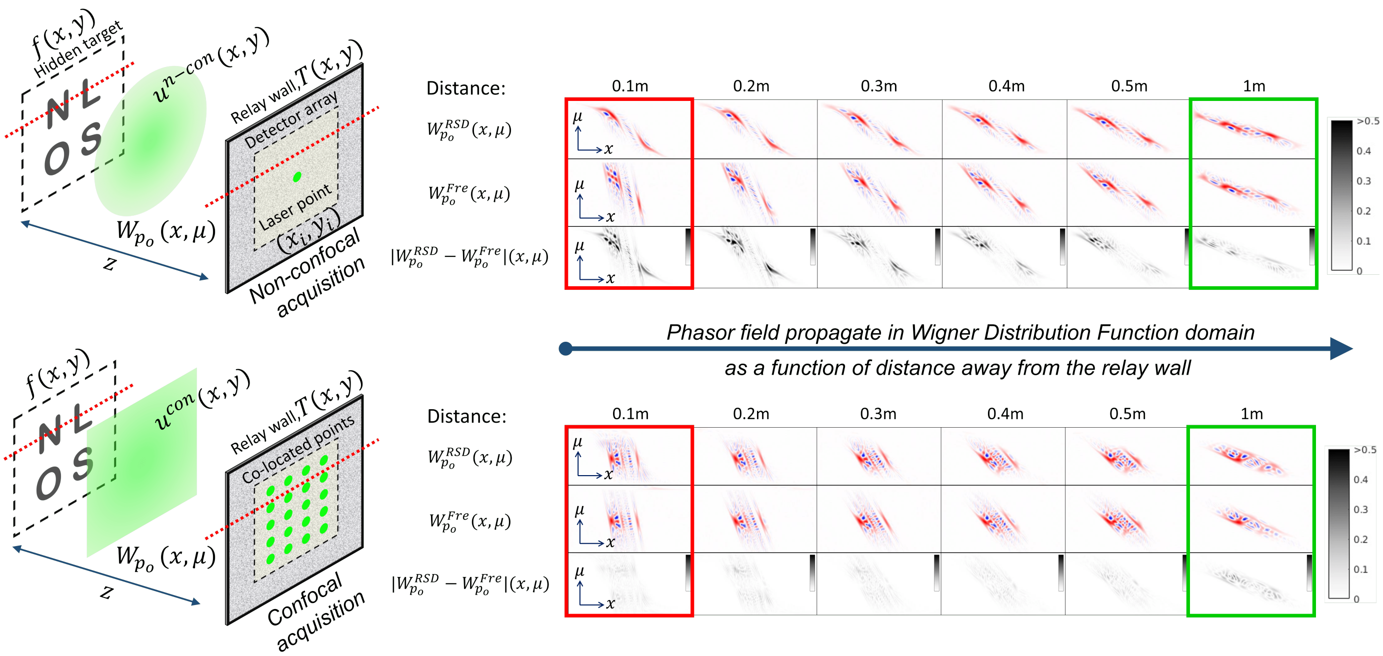

Fig. 4. Difference between the RSD and the Fresnel propagation in the WDF domain with Non-confocal, confocal acquisitionsin Eq. (18 & 19) Sec. 3.3. This numerical simulation use the same aperture function $T(x, y)$ and a input hidden target $f(x, y)$ for both non-confocal and confocal acquisitions. The non-confocal single illumination point (x_i, y_i) is at the center. Illumination functions $u^{\text{n-con}}(x, y)$ and $u^{\text{con}}(x, y)$ are shown in Eq. (18). Each row shows phasor field distributions in the WDF domain as a function of distance z. $\mathcal{W}_{p_o}^{\text{RSD}}(x, \mu)$, $\mathcal{W}_{p_o}^{\text{Fre}}(x, \mu)$ refers to the phasor field WDF distribution from the RSD or the Fresnel diffraction. For each depth, we plot the absolute difference between normalized WDF for RSD and Fresnel $|\mathcal{W}_{p_o}^{\text{RSD}} - \mathcal{W}_{p_o}^{\text{Fre}}|(x, \mu)$ (Normalized WDF's value between 0-1). The Fresnel approximation for the non-confocal and the confocal show different errors by the absolute difference map in the WDF domain (from red to green box).

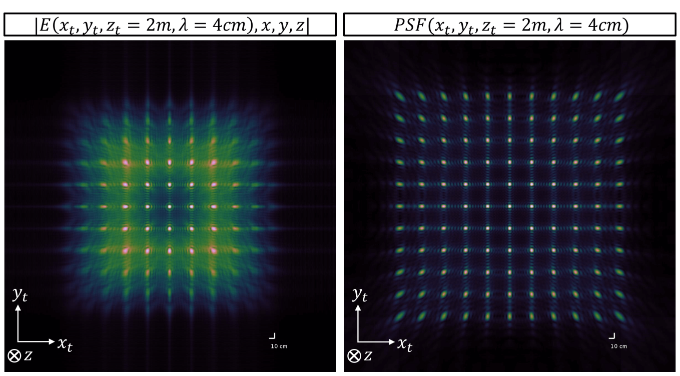

Fig. 5. Error plot for Eq. (20). $|E(x_t, y_t, z_t, x, y, z)|$ refers to complex error field magnitude. $PSF(x_t, y_t, z = 2m, \lambda = 4cm)$ stands for the ideal PSF plot from RSD propagator for referencing.

Overall, this error $E(x_t, y_t, z_t, x, y, z) \in \mathbb{C}$ leads to both magnitude and phase error in the reconstruction domain. We give an illustration of this error in magnitude in Fig. 5 using the illumination function $u^{\text{con}}(x, y)$. One can use Eq. (20) to evaluate more general situations with different error metrics depending on desired applications.

4 Applications

4.1 Aperture Coding

In Sec. 3.2, we model a scanning pattern on a relay wall as a real, non-negative aperture function $T(x, y)$ in Eq. (15, 16). In this section, we consider three types of aperture function as shown in Fig. 6. Type 1 describes a commonly used relay wall scanning pattern. Type 1 also illustrates the spatially dependent loss of resolution which is discussed in Sec. 3.2. As we start blocking half of the aperture, spatially dependent effects are shown in the reconstruction. This spatially dependent loss of resolution is also discussed in Liu *et al.* [47] as the missing cone. Type 2 uses a circular aperture. Type 3 refers to a coded aperture (a random binary pattern), which randomly discards 50, 80 or 90 percent of spatial measurements. Coded sampling can drastically decreases the timing for acquisitions by co-designing measurements and reconstructions. This can be explored in the future.

4.2 Phasor Field Wavefront Spatial Sampling

With the understanding of the lateral resolution in the Fourier domain shown in Fig. 3, we can study the optimal phasor field wavefront sampling. For example, one can come up the least amount of spatial measurements respect to the spatial sampling spacing Δ which is discussed in Sec. 3.1. $\lambda/2$ criterion as a *"safe option"* in Eq. (14) Sec. 3.1 is redundant if the same target is away from a relay wall.

The key idea is to apply the Fourier transform on captured phasor fields as shown in Eq. (21) ($\mathcal{F}^{2d}$ stands for the 2d Fourier transform, the notation setup is in Sec. 3.3). Z stands for depths, which is a distance between a hidden object $f(x, y)$ and a relay wall. By knowing the maximum frequency radius $k_{\max}(Z)$ of the captured phasor field wavefront, one can use $2 * k_{\max}(Z)$ as a spatial sampling criterion. This means for the same target but in different depth Z, one can use different spatial sampling spacing

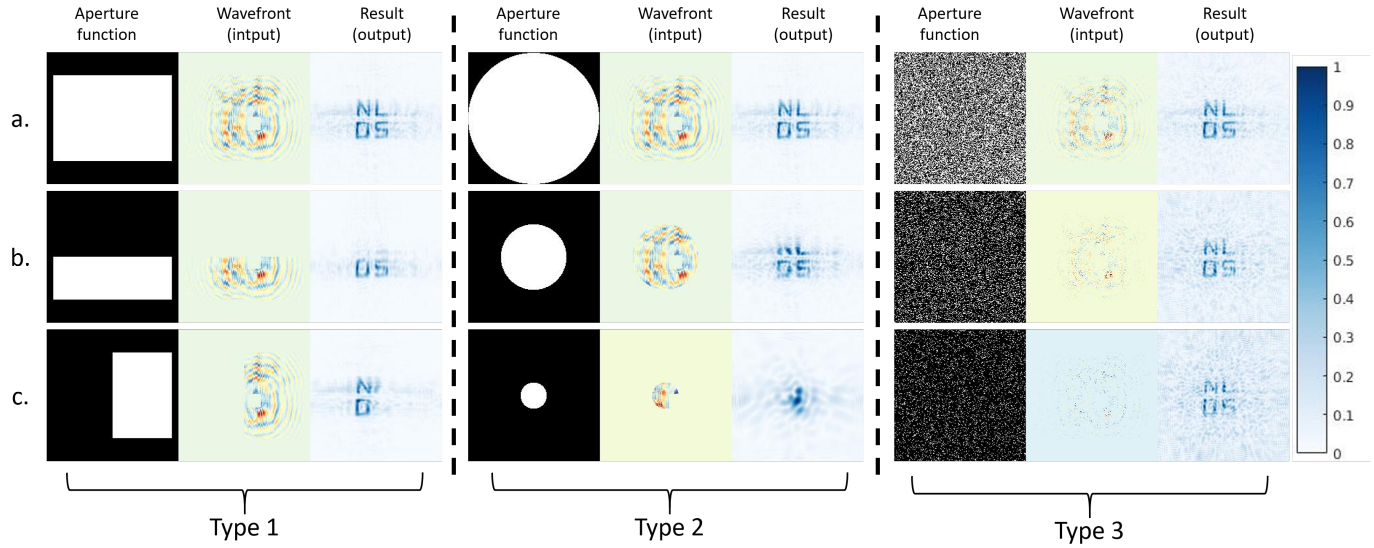

Fig. 6. Aperture coding for NLOS imaging with three examples (Type 1 to 3): Both three type examples are using the same NLOS letter dataset from Liu *et al.* [8] at central wavelength $\lambda_c = 4\,\mathrm{cm}$. For each type, we show three images (Aperture function $T(x, y)$, Phasor field wavefront input (real part) and Result (output from RSD)). Type 1 stands for a typical scanning patterns on the relay wall. Type 2 refers to a circular scanning pattern similar to Type 1. Type 3 is a random binary pattern (each element is either 0 or 1). Type 3' $T(x, y)$ is calculated from a uniform $[0, 1]$ distributed random matrix and threshold with fixed values 0.5 (Type 3 a), 0.8 (Type 3 b) and 0.9 (Type 3 c). Another words of saying this is that 50%, 80%, and 90% captured spatial signal is discarded randomly. All images are normalized individually.

Δ to sample the phasor field.

$$k_{\max}(Z) \sim \mathcal{F}^{2d}\Big[\big(\overbrace{u(x,y)}^{\text{Illumination}}\ \overbrace{f(x,y)}^{\text{Object}}\big) \underset{x-y}{*} h(x,y,Z)\Big] \tag{21}$$

With more details about noise models and prior knowledge of unknown targets, one can come up with an optimal sampling pattern (number of spatial points, spatial frequency, pattern's spatial statistical distribution, and a trade-off between acquisition time and system SNR) as a relation to the hidden target. In practice, this co-designing step might save the timing of the acquisition without loss of reconstruction qualities, become eye-safety for the acquisition by incorporating multiplexed or compressed measurement techniques.

5 Conclusion and Discussion

Our work also provides an understanding of the connections between wave optics, Wigner Distribution Function, and NLOS imaging problems. We show that the phasor field NLOS imaging method with an exact Rayleigh-Sommerfeld Diffraction operator does not have any standard geometrical interpretations in the Wigner Distribution Function domain. The achievable theoretical lateral resolution from the Rayleigh-Sommerfeld Diffraction operator is given, and it can be evaluated numerically for different settings. For analytical purposes, it is possible to use the Fresnel diffraction as an approximation to model the phasor field propagation as a shear mapping in the Wigner Distribution Function domain if errors are considered. This error is different among different acquisition schemes, and it is less for confocal than for non-confocal measurements. Thus, the Fresnel approximations can be considered on confocal measurements. The differences between the confocal and non-confocal measurements are described by adding the illumination wavefront function into the phasor field model. This means that, theoretically, one can probe a hidden object's spatial frequency contents under non-confocal acquisitions by illuminating virtual point source from different positions on the relay wall.

One can also apply concepts introduced in Sec. 2.2 to other linear NLOS imaging formation models in the Wigner Distribution Function domain. Our reliance on the Rayleigh-Sommerfeld Diffraction operator offers both advantages and disadvantages. The Rayleigh-Sommerfeld Diffraction operator is known to be hard to treat analytically. This is why past treatments of Wigner Distribution Function imaging rely on the Fresnel diffraction operator to have a simplified analytical equation. Unfortunately, this Fresnel approximation is not valid in most Non-Line-of-Sight reconstructions. Knowing theoretical limits of the exact solution is helpful, such as knowing the lateral resolution limit. Our work may stimulate further researches, such as the compressed Non-Line-of-Sight sampling, co-designing measurements and reconstruction methods, and other Non-Line-of-Sight imaging related areas.

6 Appendix

6.1 Rayleigh-Sommerfeld Diffraction and Fresnel Diffraction in the Wigner Distribution Function Domain

Consider two parallel planes with spacing z, both Rayleigh-Sommerfeld Diffraction (RSD) and Fresnel diffraction link an input wavefront $f_i(x_i)$ to a output wavefront $f_o(x_o)$ by a spatial convolution with a convolution kernel $h_{xx}(x_o, x_i)$. Because of the convolution kernel is a special case of an integral kernel, $h_{xx}(x_o, x_i)$ becomes $h_{xx}(x_o - x_i)$.

$$f_o(x_o) = f_i(x_i) * h_{xx}(x_o, x_i) = f_i(x_i) * h_{xx}(x_o - x_i)\,, \tag{22}$$

Using the Wigner Distribution Function (WDF) convolution theorem, convolution along x in spatial domain applies convolution along x but in the WDF domain. This infers Eq. (22) has a equivalent transformation in the WDF domain as follows,

$$\mathcal{W}_{f_{\mathrm{o}}}(x_{\mathrm{o}}, \mu_{\mathrm{o}}) = \mathcal{W}_h(x, \mu) \underset{x}{*} \mathcal{W}_{f_{\mathrm{i}}}(x, \mu) \tag{23}$$

Overall, there are two approaches to derive the RSD, Fresnel diffraction in the WDF domain. One is to apply WDF's convolution theorem, which means that the only thing that has to be done is to simplify $\mathcal{W}_h(x, \mu)$ given the RSD and Fresnel convolution kernel expressions. Another is to use Eq. (3,4) to derive by definitions. We show the challenge of deriving the RSD in the WDF using the first approach and derive the Fresnel diffraction in the WDF based on definitions.

For the RSD, to best of our knowledge, its kernel expression $h_{xx}(x_{\mathrm{o}} - x_{\mathrm{i}}) = \frac{e^{jk\sqrt{(x_{\mathrm{o}}-x_{\mathrm{i}})^2+z^2}}}{\sqrt{(x_{\mathrm{o}}-x_{\mathrm{i}})^2+z^2}}$ does not have a simplified analytical form in the WDF domain. In this work, we rely on numerical implementations to evaluate the RSD in the WDF domain.

As for the Fresnel diffraction, given approximations coming from a binomial expansion on the RSD kernel, it is way more easier to treat analytically. In the following, we show the Fresnel diffraction in the WDF domain by definitions following algebraic procedures in Eq. (3,4). The Fresnel spatial convolution kernel $h_{xx}(x_{\mathrm{o}} - x_{\mathrm{i}})$ can be written down as below and k stands for the wavenumber,

$$\begin{aligned} h_{xx}(x_{\mathrm{o}} - x_{\mathrm{i}}) &= \frac{e^{jkz}}{j\lambda z} \exp\Big[\frac{jk}{2z}(x_{\mathrm{o}} - x_{\mathrm{i}})^2\Big] \\ &= \alpha(z) \exp\Big[\frac{jk}{2z}(x_{\mathrm{o}} - x_{\mathrm{i}})^2\Big], \end{aligned} \tag{24}$$

Eq. (24) describes the Fresnel diffraction in its spatial representation. Use Eq. (25) to derive the integral kernel $K(x_{\mathrm{o}}, \mu_{\mathrm{o}}, x_{\mathrm{i}}, \mu_{\mathrm{i}})$ in the WDF domain as follows:

$$\begin{aligned} K(x_{\mathrm{o}}, \mu_{\mathrm{o}}, x_{\mathrm{i}}, \mu_{\mathrm{i}}) = \iint & \underbrace{h_{xx}(x_{\mathrm{o}} + \frac{x_{\mathrm{o}}^{'}}{2}, x_{\mathrm{i}} + \frac{x_{\mathrm{i}}^{'}}{2})}_{\text{term 1}} \\ & \underbrace{h_{xx}^{*}(x_{\mathrm{o}} - \frac{x_{\mathrm{o}}^{'}}{2}, x_{\mathrm{i}} - \frac{x_{\mathrm{i}}^{'}}{2})}_{\text{term 2}} \exp\Big[-j\mu_{\mathrm{o}}x_{\mathrm{o}}^{'} + j\mu_{\mathrm{i}}x_{\mathrm{i}}^{'}\Big] dx_{\mathrm{o}}^{'}dx_{\mathrm{i}}^{'}, \end{aligned} \tag{25}$$

Plug $h_{xx}(x_{\mathrm{o}}, x_{\mathrm{i}})$ from Eq. (24) into Eq. (25), simplify term 1 and term 2,

$$\begin{aligned} \text{term 1} &= \alpha(z) \exp\Big[\frac{jk}{2z}(x_{\mathrm{o}} - x_{\mathrm{i}} + \frac{x_{\mathrm{o}}^{'}}{2} - \frac{x_{\mathrm{i}}^{'}}{2})^2\Big] \\ \text{term 2} &= \exp\Big[-\frac{jk}{2z}(x_{\mathrm{o}} - x_{\mathrm{i}} - \frac{x_{\mathrm{o}}^{'}}{2} + \frac{x_{\mathrm{i}}^{'}}{2})^2\Big]\alpha^{*}(z), \end{aligned} \tag{26}$$

Plugging in terms from Eq. (26), Eq. (25) becomes,

$$\begin{aligned} & K(x_{\mathrm{o}}, \mu_{\mathrm{o}}, x_{\mathrm{i}}, \mu_{\mathrm{i}}) \\ &= \iint |\alpha(z)|^2 \exp\Big[\frac{jk}{z} \underbrace{(x_{\mathrm{o}} - x_{\mathrm{i}})(x_{\mathrm{o}}^{'} - x_{\mathrm{i}}^{'})}_{\text{use } a^2-b^2=(a+b)(a-b)}\Big] \\ & \qquad \exp\Big[-j\mu_{\mathrm{o}}x_{\mathrm{o}}^{'} + j\mu_{\mathrm{i}}x_{\mathrm{i}}^{'}\Big] dx_{\mathrm{o}}^{'}dx_{\mathrm{i}}^{'} \\ &= |\alpha(z)|^2 \int \underbrace{\int \exp\Big[\frac{jk}{z}(x_{\mathrm{o}} - x_{\mathrm{i}})x_{\mathrm{o}}^{'}\Big] \exp\Big[-j\mu_{\mathrm{o}}x_{\mathrm{o}}^{'}\Big] dx_{\mathrm{o}}^{'}}_{\text{term 3}} \\ & \qquad \exp\Big[-\frac{jk}{z}(x_{\mathrm{o}} - x_{\mathrm{i}})x_{\mathrm{i}}^{'}\Big] \exp\Big[j\mu_{\mathrm{i}}x_{\mathrm{i}}^{'}\Big] dx_{\mathrm{i}}^{'}, \end{aligned} \tag{27}$$

Simplify term 3 in Eq. (27) by using the Fourier transform property,

$$\begin{aligned} \text{term 3} &= \int \exp\Big[\frac{jk}{z}(x_{\mathrm{o}} - x_{\mathrm{i}})x_{\mathrm{o}}^{'}\Big] \exp\Big[-j\mu_{\mathrm{o}}x_{\mathrm{o}}^{'}\Big] dx_{\mathrm{o}}^{'} \\ &= 2\pi\delta(\mu_{\mathrm{o}} - \frac{k(x_{\mathrm{o}} - x_{\mathrm{i}})}{z}) \\ &= 2\pi\delta(x_{\mathrm{i}} - x_{\mathrm{o}} + \frac{z}{k}\mu_{\mathrm{o}}), \end{aligned} \tag{28}$$

Replace term 3 in Eq. (27) by Eq. (28),

$$\begin{aligned} & K(x_{\mathrm{o}}, \mu_{\mathrm{o}}, x_{\mathrm{i}}, \mu_{\mathrm{i}}) \\ &= |\alpha(z)|^2 \cdot 2\pi\delta(x_{\mathrm{i}} - x_{\mathrm{o}} + \frac{z}{k}\mu_{\mathrm{o}}) \\ & \qquad \int \mathbf{1} \cdot \exp\Big[-j(\frac{k(x_{\mathrm{o}} - x_{\mathrm{i}})}{z} - \mu_{\mathrm{i}})x_{\mathrm{i}}^{'}\Big] dx_{\mathrm{i}}^{'} \\ &= |\alpha(z)|^2 \cdot 2\pi\delta(x_{\mathrm{i}} - x_{\mathrm{o}} + \frac{z}{k}\mu_{\mathrm{o}}) \cdot 2\pi\delta(\frac{k}{z}(x_{\mathrm{o}} - x_{\mathrm{i}}) - \mu_{\mathrm{i}}), \end{aligned} \tag{29}$$

Since Eq. (29) consists of a multiplication between two delta functions, we can use it as a constraint to simplify variables,

$$\begin{cases} x_{\mathrm{i}} - x_{\mathrm{o}} + \frac{z}{k}\mu_{\mathrm{o}} = 0 \\ \frac{k}{z}(x_{\mathrm{o}} - x_{\mathrm{i}}) - \mu_{\mathrm{i}} = 0, \end{cases} \tag{30}$$

which leads to constraints $x_{\mathrm{i}} = x_{\mathrm{o}} - \frac{z}{k}\mu_{\mathrm{o}}$ and $\mu_{\mathrm{i}} = \mu_{\mathrm{o}}$.

Above all, in the WDF domain, the Fresnel diffraction integral kernel $K(x_{\mathrm{o}}, \mu_{\mathrm{o}}, x_{\mathrm{i}}, \mu_{\mathrm{i}})$ is as follows,

$$\begin{aligned} K(x_{\mathrm{o}}, \mu_{\mathrm{o}}, x_{\mathrm{i}}, \mu_{\mathrm{i}}) &= (2\pi)^2|\alpha(z)|^2\, \delta(x_{\mathrm{i}} - x_{\mathrm{o}} + \frac{z}{k}\mu_{\mathrm{o}})\, \delta(\mu_{\mathrm{i}} - \mu_{\mathrm{o}}) \\ K(x_{\mathrm{o}}, \mu_{\mathrm{o}}, x_{\mathrm{i}}, \mu_{\mathrm{i}}) &\overset{\text{normalize}}{\widehat{=}} \delta(x_{\mathrm{i}} - x_{\mathrm{o}} + \frac{z}{k}\mu_{\mathrm{o}})\, \delta(\mu_{\mathrm{i}} - \mu_{\mathrm{o}}), \end{aligned} \tag{31}$$

Using $K(x_{\mathrm{o}}, \mu_{\mathrm{o}}, x_{\mathrm{i}}, \mu_{\mathrm{i}})$ in Eq. (31) and plugging it in Eq. (3), then the corresponding input, output field WDF transformation using the Fresnel diffraction is as follows,

$$\begin{aligned} & \mathcal{W}_{f_{\mathrm{o}}}(x_{\mathrm{o}}, \mu_{\mathrm{o}}) \\ &= \frac{1}{2\pi}\iint K(x_{\mathrm{o}}, \mu_{\mathrm{o}}, x_{\mathrm{i}}, \mu_{\mathrm{i}})\mathcal{W}_{f_{\mathrm{i}}}(x_{\mathrm{i}}, \mu_{\mathrm{i}})\, dx_{\mathrm{i}}d\mu_{\mathrm{i}} \\ &\propto \iint \delta(x_{\mathrm{i}} - x_{\mathrm{o}} + \frac{z}{k}\mu_{\mathrm{o}})\delta(\mu_{\mathrm{i}} - \mu_{\mathrm{o}})\mathcal{W}_{f_{\mathrm{i}}}(x_{\mathrm{i}}, \mu_{\mathrm{i}})\, dx_{\mathrm{i}}d\mu_{\mathrm{i}}, \end{aligned} \tag{32}$$

Finally, applying constraints on variables for Eq. (32) leads to a shear mapping in the WDF domain,

$$\mathcal{W}_{f_{\mathrm{o}}}(x, \mu) = \mathcal{W}_{f_{\mathrm{i}}}(x - \frac{z}{k}\mu, \mu), \tag{33}$$

Acknowledgments

We thank anonymous Reviewer 2 (Reviewer#5) for valuable suggesting clarifications on Eq. (19) about resolution behaviors between confocal and non-confocal measurements. This work was funded by DARPA through the DARPA REVEAL project (HR0011-16-C-0025), the NASA NIAC program, and the AFOSR through the Young Investigator Program (FA9550-15-1-0208).

References

[1] R. Ramesh and J. Davis, "5D time-light transport matrix: What can we reason about scene properties?" *MIT Technical Report*, 2008. [Online]. Available: http://hdl.handle.net/1721.1/67888 1

[2] A. Kirmani, T. Hutchison, J. Davis, and R. Raskar, "Looking around the corner using ultrafast transient imaging," *International journal of computer vision*, vol. 95, no. 1, pp. 13–28, 2011. 1

[3] A. Velten, T. Willwacher, O. Gupta, A. Veeraraghavan, M. G. Bawendi, and R. Raskar, "Recovering three-dimensional shape around a corner using ultrafast time-of-flight imaging," *Nature Communications*, vol. 3, p. 745, 2012. 1, 2, 5, 7

[4] O. Gupta, T. Willwacher, A. Velten, A. Veeraraghavan, and R. Raskar, "Reconstruction of hidden 3D shapes using diffuse reflections." *Optics Express*, vol. 20, no. 17, pp. 19 096–108, Aug 2012. 1

[5] M. Buttafava, J. Zeman, A. Tosi, K. Eliceiri, and A. Velten, "Non-line-of-sight imaging using a time-gated single photon avalanche diode," *Optics Express*, vol. 23, no. 16, pp. 20 997–21 011, 2015. 1

[6] M. O'Toole, D. B. Lindell, and G. Wetzstein, "Confocal non-line-of-sight imaging based on the light-cone transform," *Nature*, vol. 555, no. 7696, p. 338, 2018. 1, 2, 7

[7] D. B. Lindell, G. Wetzstein, and M. O'Toole, "Wave-based non-line-of-sight imaging using fast f-k migration," *ACM Trans. Graph. (SIGGRAPH)*, vol. 38, no. 4, p. 116, 2019. 1, 2, 7

[8] X. Liu, I. Guillén, M. La Manna, J. H. Nam, S. A. Reza, T. H. Le, A. Jarabo, D. Gutierrez, and A. Velten, "Non-line-of-sight imaging using phasor-field virtual wave optics," *Nature*, vol. 572, no. 7771, pp. 620–623, 2019. 1, 2, 4, 5, 6, 9

[9] S. Xin, S. Nousias, K. Kutulakos, A. Sankaranarayanan, S. Narasimhan, and I. Gkioulekas, "A theory of Fermat paths for non-line-of-sight shape reconstruction," in *Proceedings of the IEEE Conference on Computer Vision and Pattern Recognition*, 2019, pp. 6800–6809. 1, 2

[10] B. Ahn, A. Dave, A. Veeraraghavan, I. Gkioulekas, and A. C. Sankaranarayanan, "Convolutional approximations to the general non-line-of-sight imaging operator," in *The IEEE International Conference on Computer Vision (ICCV)*, October 2019. 1, 2

[11] M. Galindo, J. Marco, M. O'Toole, G. Wetzstein, D. Gutierrez, and A. Jarabo, "A dataset for benchmarking time-resolved non-line-of-sight imaging," in *International Conference on Computational Photography (ICCP)*. IEEE, 2019. [Online]. Available: https://graphics.unizar.es/nlos 1, 2

[12] S. A. Reza, M. La Manna, S. Bauer, and A. Velten, "Phasor field waves: A huygens-like light transport model for non-line-of-sight imaging applications," *Optics Express*, vol. 27, no. 20, pp. 29 380–29 400, 2019. 1, 2, 4

[13] J. Dove and J. H. Shapiro, "Paraxial theory of phasor-field imaging," *Opt. Express*, vol. 27, no. 13, pp. 18 016–18 037, Jun 2019. [Online]. Available: http://www.opticsexpress.org/abstract.cfm?URI=oe-27-13-18016 1, 2, 4, 5

[14] J. A. Teichman, "Phasor field waves: a mathematical treatment," *Optics Express*, vol. 27, no. 20, pp. 27 500–27 506, 2019. 1, 2, 4

[15] S. A. Reza, M. La Manna, S. Bauer, and A. Velten, "Phasor field waves: experimental demonstrations of wave-like properties," *Optics Express*, vol. 27, no. 22, pp. 32 587–32 608, 2019. 1, 2, 4

[16] X. Liu, S. Bauer, and A. Velten, "Phasor field diffraction based reconstruction for fast non-line-of-sight imaging systems," *Nature Communications*, 2020. [Online]. Available: http://doi.org/10.1038/s41467-020-15157-4 1, 2, 4, 5

[17] E. P. Wigner, "On the quantum correction for thermodynamic equilibrium," in *Part I: Physical Chemistry. Part II: Solid State Physics*. Springer, 1997, pp. 110–120. 1

[18] P. M. Woodward, *Probability and Information Theory, with Applications to Radar: International Series of Monographs on Electronics and Instrumentation*. Elsevier, 2014, vol. 3. 1

[19] M. Testorf, B. Hennelly, and J. Ojeda-Castañeda, *Phase-Space Optics: Fundamentals and Applications: Fundamentals and Applications*. McGraw Hill Professional, 2009. 1

[20] M. J. Bastiaans, "Application of the wigner distribution function to partially coherent light," *JOSA A*, vol. 3, no. 8, pp. 1227–1238, 1986. 1

[21] M. J. Bastiaans, "The wigner distribution function applied to optical signals and systems," *Optics communications*, vol. 25, no. 1, pp. 26–30, 1978. 1

[22] M. J. Bastiaans, "Application of the wigner distribution function in optics," *The Wigner Distribution—Theory and Applications in Signal Processing*, pp. 375–426, 1997. 1, 3

[23] H. M. Ozaktas, Z. Zalevsky, and M. A. Kutay, *The Fractional Fourier Transform with applications in optics and signal processing*. Wiley, 2001. 1, 3

[24] W. D. Furlan, M. Martínez-Corral, B. Javidi, and G. Saavedra, "Analysis of 3-d integral imaging displays using the wigner distribution," *Journal of Display Technology*, vol. 2, no. 2, pp. 180–185, 2006. 1

[25] R. Ziegler, S. Bucheli, L. Ahrenberg, M. Magnor, and M. Gross, "A bidirectional light field-hologram transform," in *Computer Graphics Forum*, vol. 26, no. 3. Wiley Online Library, 2007, pp. 435–446. 1

[26] Z. Zhang and M. Levoy, "Wigner distributions and how they relate to the light field," in *2009 IEEE International Conference on Computational Photography (ICCP)*. IEEE, 2009, pp. 1–10. 1

[27] R. Horstmeyer, S. B. Oh, and R. Raskar, "Iterative aperture mask design in phase space using a rank constraint," *Optics express*, vol. 18, no. 21, pp. 22 545–22 555, 2010. 1

[28] A. Sommerfeld, *Electrodynamics: lectures on theoretical physics*. Academic Press, 2013, vol. 3. 1

[29] J. W. Goodman, *Introduction to Fourier optics*. Roberts and Company Publishers, 2005. 1, 3

[30] M. Born and E. Wolf, *Principles of optics: electromagnetic theory of propagation, interference and diffraction of light*. Elsevier, 2013. 1

[31] C.-Y. Tsai, K. N. Kutulakos, S. G. Narasimhan, and A. C. Sankaranarayanan, "The geometry of first-returning photons for non-line-of-sight imaging," in *IEEE International Conference on Computer Vision and Pattern Recognition (CVPR)*, 2017, pp. 7216–7224. 2

[32] M. La Manna, F. Kine, E. Breitbach, J. Jackson, T. Sultan, and A. Velten, "Error backprojection algorithms for non-line-of-sight imaging," *IEEE Transactions on Pattern Analysis and Machine Intelligence*, vol. 41, no. 7, pp. 1615–1626, 2018. 2

[33] C.-Y. Tsai, A. Sankaranarayanan, and I. Gkioulekas, "Beyond volumetric albedo – a surface optimization framework for non-line-of-sight imaging," in *Proceedings of the IEEE Conference on Computer Vision and Pattern Recognition*, 2019, pp. 1545–1555. 2

[34] J. Iseringhausen and M. B. Hullin, "Non-line-of-sight reconstruction using efficient transient rendering," *arXiv preprint arXiv:1809.08044*, 2018. 2

[35] V. Arellano, D. Gutierrez, and A. Jarabo, "Fast back-projection for non-line of sight reconstruction," *Optics Express*, vol. 25, no. 10, pp. 11 574–11 583, 2017. 2

[36] M. Laurenzis and A. Velten, "Feature selection and back-projection algorithms for nonline-of-sight laser–gated viewing," *Journal of Electronic Imaging*, vol. 23, no. 6, p. 063003, 2014. 2

[37] C. Thrampoulidis, G. Shulkind, F. Xu, W. T. Freeman, J. H. Shapiro, A. Torralba, F. N. Wong, and G. W. Wornell, "Exploiting occlusion in non-line-of-sight active imaging," *IEEE Transactions on Computational Imaging*, vol. 4, no. 3, pp. 419–431, 2018. 2

[38] F. Xu, G. Shulkind, C. Thrampoulidis, J. H. Shapiro, A. Torralba, F. N. Wong, and G. W. Wornell, "Revealing hidden scenes by photon-efficient occlusion-based opportunistic active imaging," *Optics express*, vol. 26, no. 8, pp. 9945–9962, 2018. 2

[39] F. Heide, M. O'Toole, K. Zang, D. Lindell, S. Diamond, and G. Wetzstein, "Non-line-of-sight imaging with partial occluders and surface normals," *ACM Trans. Graph.*, 2019. 2

[40] A. Pediredla, A. Dave, and A. Veeraraghavan, "SNLOS: Non-line-of-sight scanning through temporal focusing," in *International Conference on Computational Photography*, vol. 1, 2019. 2

[41] A. K. Pediredla, M. Buttafava, A. Tosi, O. Cossairt, and A. Veeraraghavan, "Reconstructing rooms using photon echoes: A plane based model and reconstruction algorithm for looking around the corner," in *2017 IEEE International Conference on Computational Photography (ICCP)*. IEEE, 2017, pp. 1–12. 2

[42] J. Brooks and D. Faccio, "A single-shot non-line-of-sight range-finder," *Sensors*, vol. 19, no. 21, p. 4820, 2019. 2

[43] L. Huang, X. Wang, Y. Yuan, S. Gu, and Y. Shen, "Improved algorithm of non-line-of-sight imaging based on the Bayesian statistics," *JOSA A*, vol. 36, no. 5, pp. 834–838, 2019. 2

[44] J. Klein, M. Laurenzis, D. L. Michels, and M. B. Hullin, "A quantitative platform for non-line-of-sight imaging problems," in *British Machine Vi-*

sion Conference 2018, BMVC 2018, Northumbria University, Newcastle, UK, September 3-6, 2018, 2018, p. 104. 2

[45] G. Musarra, A. Lyons, E. Conca, Y. Altmann, F. Villa, F. Zappa, M. Padgett, and D. Faccio, "Non-line-of-sight 3D imaging with a single-pixel camera," *arXiv preprint arXiv:1903.04812*, 2019. 2

[46] G. Musarra, A. Lyons, E. Conca, F. Villa, F. Zappa, Y. Altmann, and D. Faccio, "3D RGB non-line-of-sight single-pixel imaging," in *Imaging and Applied Optics 2019 (COSI, IS, MATH, pcAOP)*. Optical Society of America, 2019, p. IM2B.5. [Online]. Available: http://www.osapublishing.org/abstract.cfm?URI=ISA-2019-IM2B.5 2

[47] X. Liu, S. Bauer, and A. Velten, "Analysis of feature visibility in non-line-of-sight measurements," in *Proceedings of the IEEE Conference on Computer Vision and Pattern Recognition*, 2019, pp. 10 140–10 148. 2, 8

[48] M. Laurenzis, "Shadows used to peer around corners," 2019. 2

[49] T. Maeda, G. Satat, T. Swedish, L. Sinha, and R. Raskar, "Recent advances in imaging around corners," *arXiv preprint arXiv:1910.05613*, 2019. 2

[50] M. Laurenzis, J. Klein, E. Bacher, and S. Schertzer, "Approaches to solve inverse problems for optical sensing around corners," in *Emerging Imaging and Sensing Technologies for Security and Defence IV*, vol. 11163. International Society for Optics and Photonics, 2019, p. 1116304. 2

[51] M. La Manna, X. Liu, J.-H. Nam, M. Laurenzis, and A. Velten, "A line-of-sight approach for non-line-of-sight imaging (conference presentation)," in *Computational Imaging IV*, vol. 10990. International Society for Optics and Photonics, 2019, p. 1099005. 2

[52] F. Heide, L. Xiao, W. Heidrich, and M. B. Hullin, "Diffuse mirrors: 3D reconstruction from diffuse indirect illumination using inexpensive time-of-flight sensors," in *Proceedings of the IEEE Conference on Computer Vision and Pattern Recognition*, 2014, pp. 3222–3229. 2

[53] O. Katz, P. Heidmann, M. Fink, and S. Gigan, "Non-invasive single-shot imaging through scattering layers and around corners via speckle correlations," *Nature photonics*, vol. 8, no. 10, p. 784, 2014. 2

[54] B. M. Smith, M. O'Toole, and M. Gupta, "Tracking multiple objects outside the line of sight using speckle imaging," in *Proceedings of the IEEE Conference on Computer Vision and Pattern Recognition*, 2018, pp. 6258–6266. 2

[55] J. Boger-Lombard and O. Katz, "Passive optical time-of-flight for non line-of-sight localization," *Nature communications*, vol. 10, 2019. 2

[56] W. Chen, S. Daneau, F. Mannan, and F. Heide, "Steady-state non-line-of-sight imaging," in *The IEEE Conference on Computer Vision and Pattern Recognition (CVPR)*, June 2019, pp. 6790–6799. 2

[57] J. Klein, C. Peters, J. Martín, M. Laurenzis, and M. B. Hullin, "Tracking objects outside the line of sight using 2d intensity images," *Scientific reports*, vol. 6, p. 32491, 2016. 2

[58] F. Willomitzer, F. Li, M. M. Balaji, P. Rangarajan, and O. Cossairt, "High resolution non-line-of-sight imaging with superheterodyne remote digital holography," in *Computational Optical Sensing and Imaging*. Optical Society of America, 2019, pp. CM2A–2. 2

[59] P. Rangarajan, F. Willomitzer, O. Cossairt, and M. P. Christensen, "Spatially resolved indirect imaging of objects beyond the line of sight," in *Unconventional and Indirect Imaging, Image Reconstruction, and Wavefront Sensing 2019*, vol. 11135. International Society for Optics and Photonics, 2019, p. 111350I. 2

[60] F. Willomitzer, P. V. Rangarajan, F. Li, M. M. Balaji, M. P. Christensen, and O. Cossairt, "Synthetic wavelength holography: An extension of gabor's holographic principle to imaging with scattered wavefronts," *arXiv preprint arXiv:1912.11438*, 2019. 2

[61] C. A. Metzler, F. Heide, P. Rangarajan, M. M. Balaji, A. Viswanath, A. Veeraraghavan, and R. G. Baraniuk, "Deep-inverse correlography: towards real-time high-resolution non-line-of-sight imaging," *Optica*, vol. 7, no. 1, pp. 63–71, 2020. 2

[62] D. B. Lindell, G. Wetzstein, and V. Koltun, "Acoustic non-line-of-sight imaging," in *Proceedings of the IEEE Conference on Computer Vision and Pattern Recognition*, 2019, pp. 6780–6789. 2

[63] S. Divitt, D. F. Gardner, and A. T. Watnik, "Seeing around corners in the mid-infrared using speckle imaging," in *Frontiers in Optics*. Optical Society of America, 2019, pp. FTh3F–3. 2

[64] T. Maeda, Y. Wang, R. Raskar, and A. Kadambi, "Thermal non-line-of-sight imaging," in *2019 IEEE International Conference on Computational Photography (ICCP)*. IEEE, 2019, pp. 1–11. 2

[65] M. J. Bastiaans, "The wigner distribution function and its applications to optics," in *AIP conference proceedings*, vol. 65, no. 1. AIP, 1980, pp. 292–312. 3

[66] F. Shen and A. Wang, "Fast-Fourier-transform based numerical integration method for the rayleigh-sommerfeld diffraction formula," *Applied optics*, vol. 45, no. 6, pp. 1102–1110, 2006. 3

[67] V. Nascov and P. C. Logofătu, "Fast computation algorithm for the Rayleigh-Sommerfeld diffraction formula using a type of scaled convolution," *Applied optics*, vol. 48, no. 22, pp. 4310–4319, 2009. 3

[68] M. Fink, "Time-reversed acoustics," *Scientific American*, vol. 281, no. 5, pp. 91–97, 1999. 5

Xiaochun Liu received the BE degree in Measurement Control and Optical Instrumentation from Changchun University of Science and Technology, China. Since 2017, he is a PhD student in the Department of Electrical and Computer Engineering, University of Wisconsin-Madison. His research interest is in Computational Imaging.

Andreas Velten received the BA degree in physics from the Julius Maximilian University of Wurzburg, Wurzburg, Germany, in 2003, and the PhD degree in physics from the University of New Mexico, Albuquerque, NM, in 2009. From 2010 to 2012, he was a postdoctoral research associate with the Massachusetts Institute of Technology (Cambridge, MA) working on high speed imaging systems that can look around a corner using scattered light. From 2013 to 2016, he was an associate scientist with the Laboratory for Optical and Computational Instrumentation, University of Wisconsin–Madison (Madison WI), working in optics, computational imaging, and medical devices. Since 2016, he is an assistant professor with the Biostatistics and Medical Informatics, Electrical and Computer Engineering Department, University of Wisconsin–Madison. His research focuses on performing multidisciplinary work in applied computational optics and imaging.